Intramuscular EMG-driven Musculoskeletal Modelling: Towards Implanted Muscle Interfacing in Spinal Cord Injury Patients

Citation for the original published paper (version of record):
Jung, M., Muceli, S., Rodrigues, C. et al (2021)
Intramuscular EMG-driven Musculoskeletal Modelling: Towards Implanted Muscle Interfacing in Spinal Cord Injury Patients
IEEE Transactions on Biomedical Engineering, In Press
http://dx.doi.org/10.1109/TBME.2021.3087137

(article starts on next page)

This article has been accepted for publication in a future issue of this journal, but has not been fully edited. Content may change prior to final publication. Citation information: DOI 10.1109/TBME.2021.3087137, IEEE Transactions on Biomedical Engineering

TBME-02406-2020.R1

Intramuscular EMG-driven Musculoskeletal Modelling: Towards Implanted Muscle Interfacing in Spinal Cord Injury Patients

Moon Ki Jung, Silvia Muceli, *Senior Member, IEEE*, Camila Rodrigues, Álvaro Megía-García, Alejandro Pascual-Valdunciel, *Member, IEEE*, Antonio J. del-Ama, Angel Gil-Agudo, Juan C. Moreno, *Senior Member, IEEE*, Filipe Oliveira Barroso, *Member, IEEE*, José Luis Pons, *Senior Member, IEEE*, and Dario Farina, *Fellow, IEEE*

***Abstract*— *Objective:* Surface EMG-driven modelling has been proposed as a means to control assistive devices by estimating joint torques. Implanted EMG sensors have several advantages over wearable sensors but provide a more localized information on muscle activity, which may impact torque estimates. Here, we tested and compared the use of surface and intramuscular EMG measurements for the estimation of required assistive joint torques using EMG driven modelling. *Methods:* Four healthy subjects and three incomplete spinal cord injury (SCI) patients performed walking trials at varying speeds. Motion capture marker trajectories, surface and intramuscular EMG, and ground reaction forces were measured concurrently. Subject-specific musculoskeletal models were developed for all subjects, and inverse dynamics analysis was performed for all individual trials. EMG-driven modelling based joint torque estimates were obtained from surface and intramuscular EMG. *Results:* The correlation between the experimental and predicted joint torques was similar when using intramuscular or surface EMG as input to the EMG-driven modelling estimator in both healthy individuals and patients. *Conclusion:* We have provided the first comparison of non-invasive and implanted EMG sensors as input signals for torque estimates in healthy individuals and SCI patients. *Significance:* Implanted EMG sensors have the potential to be used as a reliable input for assistive exoskeleton joint torque actuation.**

***Index Terms*—EMG driven modelling, musculoskeletal model, electromyography, assistive technology, human-machine interface, spinal cord injury**

I. Introduction

THERE has been growing interest in powered wearable assistive devices that can increase the physical performance of users. One of their application is for neurorehabilitation, where this technology can enhance the motor capabilities of neurologically impaired individuals, such as stroke or spinal cord injury (SCI) patients, thus accelerating the recovery process and minimizing functional disability. Among the activities of daily living (ADL), walking is one of the most demanded and directly affects quality of life.

Human-machine interfaces (HMI) based on myoelectric control provide the decoding of human motor intention from electromyographic (EMG) signals and translate them into high level commands for controlling prostheses or exoskeletons [1], [2]. One of the major challenges of EMG-based HMIs is to decode the intention to activate multiple degrees of freedom (DOFs) in a coordinated manner to replicate natural human movements [3], [4]. Among various myoelectric HMIs, EMG-driven neuromusculoskeletal (NMS) modelling approaches have been developed to estimate user-intended joint moments [5], [6], [7], [8], [9], [10]. These systems can operate in real-time [11] and be applied to control exoskeletons and prostheses [12], [13], [14].

In most of the existing EMG-driven model-based HMIs, surface EMG (sEMG) signals are typically acquired from multiple muscles and used to derive individual muscle

This work was funded by the European Union's Horizon 2020 research and innovation program (Project EXTEND—Bidirectional Hyper-Connected Neural System) under grant agreement No 779982.

M. K. Jung and D. Farina are with the Department of Bioengineering, Imperial College London. UK (e-mail: m.jung@imperial.ac.uk; d.farina@imperial.ac.uk).

S. Muceli is with the Division of Signal Processing and Biomedical Engineering, Department of Electrical Engineering, Chalmers University of Technology, Göteborg, Sweden (e-mail: muceli@chalmers.se).

C. Rodrigues, A. Pascual-Valdunciel, J. C. Moreno and F. O. Barroso are with the Neural Rehabilitation Group, Cajal Institute, Spanish National Research Council (CSIC), Madrid, Spain. (e-mail: camila.rodrigues@cajal.csic.es; alejandropv@cajal.csic.es; jc.moreno@csic.es; filipe.barroso@cajal.csic.es).

Á. Megía-García and A. Gil-Agudo are with the Biomechanics and Assistive Technology Unit, National Hospital for Paraplegics. Unit of Neurorehabilitation, Biomechanics and Sensory-Motor Function (HNP-SESCAM), Unit associated to the CSIC, Toledo, Spain. (e-mail: amegiag@externas.sescam.jccm.es; amgila@sescam.jccm.es).

A. J. del-Ama is with the Rey Juan Carlos University and the Biomechanics and Assistive Technology Unit, National Hospital for Paraplegics, Spain. (e-mail: antonio.delama@urjc.es).

J. L. Pons is with the Neural Rehabilitation Group, Cajal Institute, Spanish National Research Council (CSIC), Madrid, Spain, the Legs & Walking AbilityLab, Shirley Ryan AbilityLab, Chicago, IL, United States; the Department of Biomedical Engineering and Mechanical Engineering, McCormick School of Engineering, Northwestern University, Chicago, IL, United States; and the Department of PM&R, Feinberg School of Medicine, Northwestern University, Chicago, IL, United States (e-mail: jpons@sralab.org).

This article has been accepted for publication in a future issue of this journal, but has not been fully edited. Content may change prior to final publication. Citation information: DOI 10.1109/TBME.2021.3087137, IEEE Transactions on Biomedical Engineering

activation signals in order to calculate their contributions to joint moments. While sEMG is a non-invasive, and therefore convenient, interface technology, it has limitations in its translational potential, mainly due to the need to replace the electrodes at each use of the interface. This issue is associated to the need for recalibration of the HMI, as it has been extensively documented for myoelectric prostheses (e.g., [15], [16], [17]). On the other hand, intramuscular EMG (iEMG) provides recordings from implanted sensors. Human intramuscular implants have been developed and tested chronically in patients for the control of prostheses [18] but have not been extensively explored for the control of exoskeletons. Compared to sEMG, iEMG can provide a chronic interface. Moreover, the surgical procedures for chronic implants in muscles are relatively simple.

iEMG is usually more selective than surface EMG. Selectivity may have the advantage of reducing crosstalk between multi-muscle EMG recordings [19] but also implies that the recording is potentially less representative of the global muscle activity. These characteristics of iEMG may influence the estimation quality of EMG-driven NMS model-based HMI. Some previous studies compared the control performance of sEMG and iEMG in the field of prosthetics. For example, sEMG and iEMG have been compared in the 2DOFs wrist joint torque estimation using an artificial neural network in healthy subjects [20]. Another research [21] compared the performance of a real-time virtual posture matching task using a musculoskeletal model-based control algorithm from sEMG and iEMG in both healthy and amputee subjects. In other studies, it has been shown that there is a good agreement in the linear envelope profiles of sEMG and iEMG recorded from ankle dorsi and plantar flexors during walking [22]. sEMG and iEMG recorded from different muscles have been used in combination as inputs for EMG-driven NMS models of the shoulder joint DOFs, but sEMG and iEMG were not recorded concurrently from the same muscles so that it was not possible to compare the performance of EMG-driven modelling between sEMG and iEMG [23].

Several studies have shown that muscle activation patterns of SCI patients differ from those of healthy individuals. For examples, difference in muscle activations in incomplete SCI (iSCI) patients were observed for the tibialis anterior during the stance phase of gait cycle and for the rectus femoris during the swing phase [24]. Another study showed a greater number of motor modules (also known as muscle synergies) in healthy individuals than in the most affected side of iSCI patients during walking [25]. These differences in EMG patterns of iSCI patients may affect the performance of EMG-driven NMS modeling. To the best of our knowledge, there are no previous studies that tested the performance of EMG-driven NMS modelling when using iEMG with lower body kinematics and kinetics in neurologically impaired patients.

The aim of this study is to validate the iEMG-driven NMS model as an implanted interface on SCI patients for assistive exoskeleton control. For this purpose, we used both sEMG and iEMG measurements to estimate the performance of iEMG-driven NMS model's joint torque prediction compared to the baseline reference (sEMG-driven NMS model). We applied this approach in both healthy individuals and iSCI patients.

TABLE I
SUMMARY OF SUBJECTS

ID	GENDER	AGE [years]	WEIGHT [kg]	HEIGHT [m]
H01	F	22	66	1.64
H02	M	27	60	1.69
H03	F	22	60	1.69
H04	M	21	68	1.71
P01	M	56	63	1.63
P02	M	56	90	1.79
P03	M	47	74	1.83

Summary of both healthy (H01-H04) and iSCI (P01-P03) subjects in the experiments.

TABLE II
SUMMARY OF CLINICAL INFORMATION OF ISCI SUBJECTS

ID	AIS	LEVEL OF INJURY	TIME SINCE INJURY [months]	ETIOLOGY
P01	D	C4	6	Vascular
P02	D	L1	4	Inflammatory
P03	D	C4	7	Traumatic

Summary of clinical information of iSCI (P01-P03) subjects. AIS stands for American Spinal Injury Association Impairment Scale (AIS).

II. EXPERIMENTS

A. Participants

4 healthy and 3 incomplete SCI subjects participated to the experiment. All subjects gave their written informed consent to the procedures of the study, approved by the Ethic Committee of the National Hospital for Spinal Cord Injury of Toledo (Ref. No. 724; 17/12/2018), where the experiments were conducted. Table I summaries the information of all subjects, and Table II shows the clinical information about iSCI patients in detail. All iSCI patients were able to walk without any external aid.

B. Experimental procedure

For both healthy and iSCI subjects, 5 static trials were recorded for each subject. Subjects were asked to stand with their arms crossed on the chest at rest. One of these static trials was selected randomly to create a subject-specific geometrically scaled human musculoskeletal model using a template model (gait 2392) in OpenSim version 3.3 [26]. After these static trials, dynamic trials were recorded. Healthy subjects performed self-paced walking trials at three speeds: normal, slow and very slow. For each speed, 4 trials were acquired. iSCI subjects performed 10 self-paced walking trials at one speed.

C. Data acquisition

We concurrently recorded kinematic and EMG data during the static and walking trials. We also measured ground reaction forces during walking. Additionally, we recorded a trigger signal to allow offline synchronization of the EMG and kinematic data. Surface and intramuscular EMG signals were

This article has been accepted for publication in a future issue of this journal, but has not been fully edited. Content may change prior to final publication. Citation information: DOI 10.1109/TBME.2021.3087137, IEEE Transactions on Biomedical Engineering

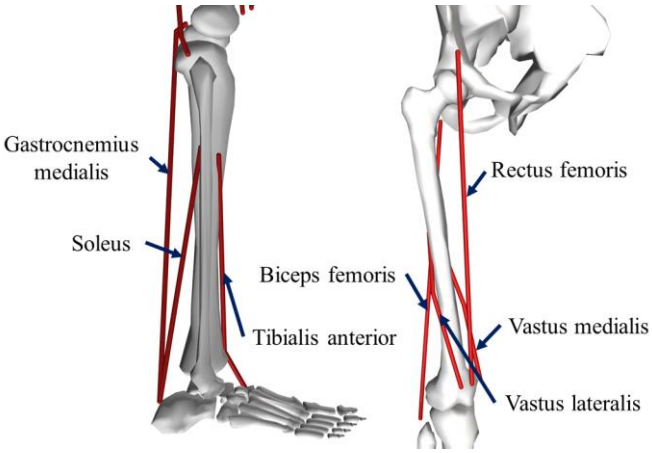

Fig. 1. Muscles were both surface and intramuscular EMG electrodes were positioned.

acquired from 7 muscles of the right leg: tibialis anterior, gastrocnemius medialis, soleus, vastus lateralis, vastus medialis, rectus femoris and biceps femoris (Fig. 1). Both surface and intramuscular EMG signals were acquired from each of these muscles in bipolar derivation with a multi-channel amplifier (Quattrocento, OTbioelettronica, Turin, Italy) that provided a gain of 150 and sampled the signals at 10240 Hz with 16-bit resolution. Surface EMG was recorded with a pair of Ag/AgCl electrodes (Ambu® Neuroline 720 01-K/12, Ambu A/S, Ballerup, Denmark) with inter-electrode distance of 22 mm in each muscle. Intramuscular signals were acquired with a pair of fine wires (Fi-Wi2, OTbioelettronica, Turin, Italy) inserted in the target muscle with an insertion angle of approximately 45°. The wires were inserted with a 25G hypodermic needle that was removed after the insertion, leaving the wires inside the muscle for the recordings. The uninsulated part of the wire had a length of approximately 1 cm. The skin was shaved, when needed, and cleansed with alcohol before the needle insertion. The wires were secured with tape to avoid their removal by an accidental tug. The surface electrodes were placed on the area overlying the portion of the muscle were the bare ends of the wire were located. A wet band was placed at the ankle to act as a ground electrode. After securing all electrodes with tape, the leg was covered with an elastic band to minimize motion artefacts during the recordings.

Kinematics was recorded with an active-marker type motion capture system (Codamotion, Charnwood Dynamics Limited, United Kingdom) at a sampling rate of 200 Hz. Codamotion uses different types of wands for pelvis, thigh and shank, and 22 physical markers [27]. In addition to the default Codamotion marker set, 6 additional markers (CLAV: jugular notch where the clavicle meets the sternum, STRN: xiphoid process of the sternum, LSHO: left shoulder, RHSO: right shoulder, LHEE: posterior distal aspect of left heel, RHEE: posterior distal aspect of right heel) were included in the experimental protocol of dynamic trials in order to capture the kinematics of upper body segments and to improve the kinematics of both feet segments. For static trials, 10 additional markers (LTOE: location between second and third metatarsal heads in left foot, RTOE: location between second and third metatarsal heads in right foot, LMMA: left medial malleolus, RMMA: right medial malleolus, LKME: left knee medial epicondyle, RKME: right knee medial

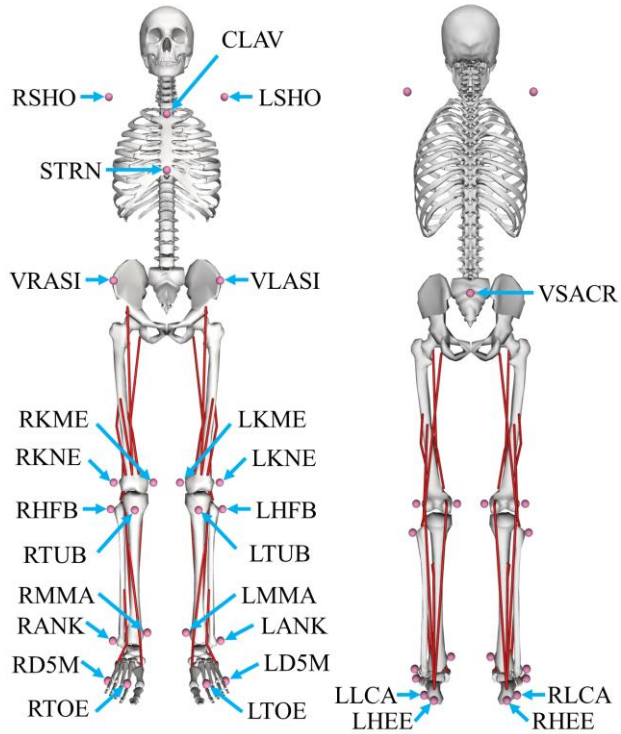

Fig. 2. Representative illustration of the static trial marker set for lower and upper body segments in both healthy and iSCI subjects.

epicondyle, LHFB: light head of fibular, RHFB: right head of fibular, LTUB: left tibial tuberosity, RTUB: right tibial tuberosity) were included in order to improve the scaling of the OpenSim musculoskeletal model. Some of the additional markers were adapted from the Oxford Foot Model [28]. All lower body markers were attached bilaterally so that inverse kinematics and inverse dynamics were performed with both legs in OpenSim. Fig. 2 shows the locations of the markers used in the static trials of the experiments.

Ground reaction forces were measured by two force plates (KISLER, Winterthur, Switzerland) at a sampling rate of 1000 Hz. In the walking trials, subjects were instructed to contact the first force plate with their right foot and the second force plate with their left foot.

D. *Data processing*

The surface (intramuscular) EMG signals were band-pass filtered at 30-450 Hz (100-4400 Hz) with a 2nd order zero-lag Butterworth filter. The resulting signals were rectified and low-pass filtered at 6 Hz (2nd order zero-lag Butterworth digital filter) to extract the envelopes. Envelopes were then down-sampled to 1000 Hz to match the sampling frequency of the data from the force plate system. For each subject and muscle, the envelopes were amplitude-normalized with respect to peak-processed values obtained from the dynamic trials. The resulting normalized EMG envelopes were regarded as experimental muscle excitations to be used as the input for the EMG-driven modelling pipeline.

Due to the complexity of the experimental procedures, there were some dropped-out markers in the motion capture marker

This article has been accepted for publication in a future issue of this journal, but has not been fully edited. Content may change prior to final publication. Citation information: DOI 10.1109/TBME.2021.3087137, IEEE Transactions on Biomedical Engineering

TABLE III
RECORDED EMG SIGNALS AND RELEVANT MODEL MUSCLE BRANCHES

Measured EMG	Relevant model muscle branches
Biceps femoris	biceps femoris long head, biceps femoris short head
Gastrocnemius medialis	gastrocnemius lateralis, gastrocnemius medialis
Soleus	soleus
Tibialis anterior	tibialis anterior, peroneus tertius
Vastus lateralis	vastus lateralis, vastus intermedius
Vastus medialis	vastus medialis, vastus intermedius
Rectus femoris	rectus femoris

Measured EMG signals and their corresponding muscle branches in the NMS model. Some muscle branches use their closest muscle's measured EMG signals. For instance, the peroneus tertius muscle branch in the musculoskeletal model used the measured EMG signal from the tibialis anterior muscle and the vastus intermedius muscle branch used the average of the vastus lateralis and vastus medialis EMG measurements.

acquisition data. Therefore, cubic spline interpolation was performed for all marker trajectories so that the missing marker data were estimated by interpolation while the original existing marker data was unchanged. After this preprocessing of the motion capture marker dataset, both motion marker trajectories and force plate measurements were low-pass filtered using a zero-lag, 2nd order, 6-Hz Butterworth filter.

The processed marker trajectories, EMG envelopes, and ground reaction forces were synchronized, and were stored in OpenSim compatible file formats so that they could be used in the EMG-driven NMS model-based joint torque estimation framework. The data processing was performed by custom-made programs using Python, NumPy and SciPy libraries [29], [30], [31].

III. EMG-DRIVEN MUSCULOSKELETAL MODEL

A. Neuromusculoskeletal (NMS) model

A generic model (gait2392) of the software OpenSim [26] was scaled to match the individual subject's anthropometry. This was done based on the marker trajectories from static motion capture trials, and the estimated locations of joint centers for the hip, knee and ankle. Musculoskeletal parameters were linearly scaled according to the change in muscle-tendon lengths. Body mass was also scaled to the individual while the relative proportions of individual segment masses were kept consistently. The OpenSim's modelling pipeline, that includes inverse kinematics, inverse dynamics and the muscle analysis tool, was used to calculate joint angles, joint moments and musculotendon unit (MTU) kinematics (muscle lengths and moments arms), for each walking trial.

B. EMG-driven modelling framework

The output from OpenSim (joint angles, muscle lengths and moment arms) and EMG-derived muscle excitations were used as the input to an EMG-driven modelling framework [9]. The EMG-driven model was used to calculate muscle forces and their relevant joint moments using muscle excitations and MTU kinematics. Full-predictive open-loop mode [9] was used in this study, because this open-loop model directly calculates the muscle forces and their resultant joint torques by using recorded EMG signals and 3D joint angles.

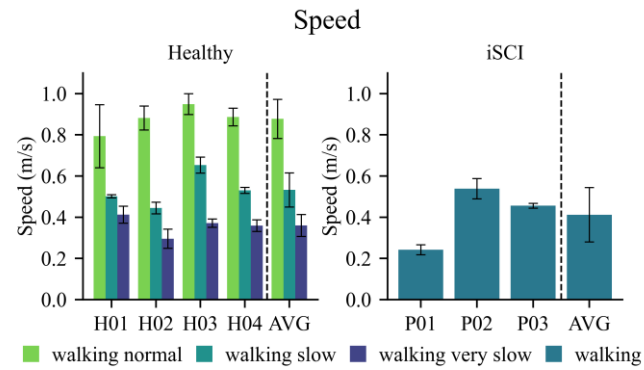

Fig. 3. Walking speeds for healthy and iSCI subjects. Healthy subjects performed the walking trials at 3 speeds (normal, slow and very slow) whereas iSCI subjects performed only single speed walking. All walking speeds were self-paced.

The first step for EMG-driven modelling is the calibration. The aim of the calibration process is to identify a set of parameters for each MTU. The first parameter set is related to the MTU's activation dynamics that determines the translation from muscle excitation to muscle activation. The neural activation, which is derived from the muscle excitation, was represented by a critically damped linear second-order differential system [9]:

$$u(t) = \alpha e(t-d) - (C_1 + C_2)u(t-1) - C_1 C_2 u(t-2) \quad (1)$$

where $u(t)$ is the neural activation, $e(t)$ is the muscle excitation at time t, α is the muscle gain coefficient, C_1 and C_2 are the recursive coefficients, and d is the electromechanical delay. The neural activation and the muscle activation are associated by a non-linear relation:

$$a(t) = \frac{e^{Au(t)} - 1}{e^{A} - 1} \quad (2)$$

where $a(t)$ is the muscle activation, and A is a non-linear shape factor, constrained in the interval $(-3, 0)$.

The second parameter set relates to the muscle-tendon contraction dynamics that transforms muscle activation and MTU kinematics into muscle force by using a Hill-type muscle model. The MTU force $F^{mt}(t)$ can be formulated as follows:

$$F^{mt}(t) = F^{t}(t) = F^{m}(t)\cos(\varphi(t)) = F^{max}\left[a(t) f_a(l^m(t)) f_v(v^m(t)) + f_p(l^m(t))\right]\cos(\varphi(t)) \quad (3)$$

where $F^t(t)$ is the tendon force, $F^m(t)$ is the fiber force, F^{max} is the maximum isometric fiber force, $a(t)$ is the muscle activation, $\varphi(t)$ is the pennation angle of the fibers, $l^m(t)$ is the normalized fiber length, $v^m(t)$ is the normalized fiber velocity, $f_a(l^m(t))$ is the fiber force-length relationship, $f_v(v^m(t))$ is the fiber force-velocity relationship, and $f_p(l^m(t))$ is the passive force-length relationship.

During the calibration process, a simulated annealing algorithm [32] was used to identify the subject-specific model parameters, including A, C_1, C_2, the tendon slack length, the optimal fiber length, and the maximum isometric fiber force [9]. The initial parameters were iteratively updated in order to minimize the mismatch between the predicted and the experimentally measured joint moments for the target DOFs. The experimental joint moments were estimated from the

This article has been accepted for publication in a future issue of this journal, but has not been fully edited. Content may change prior to final publication. Citation information: DOI 10.1109/TBME.2021.3087137, IEEE Transactions on Biomedical Engineering

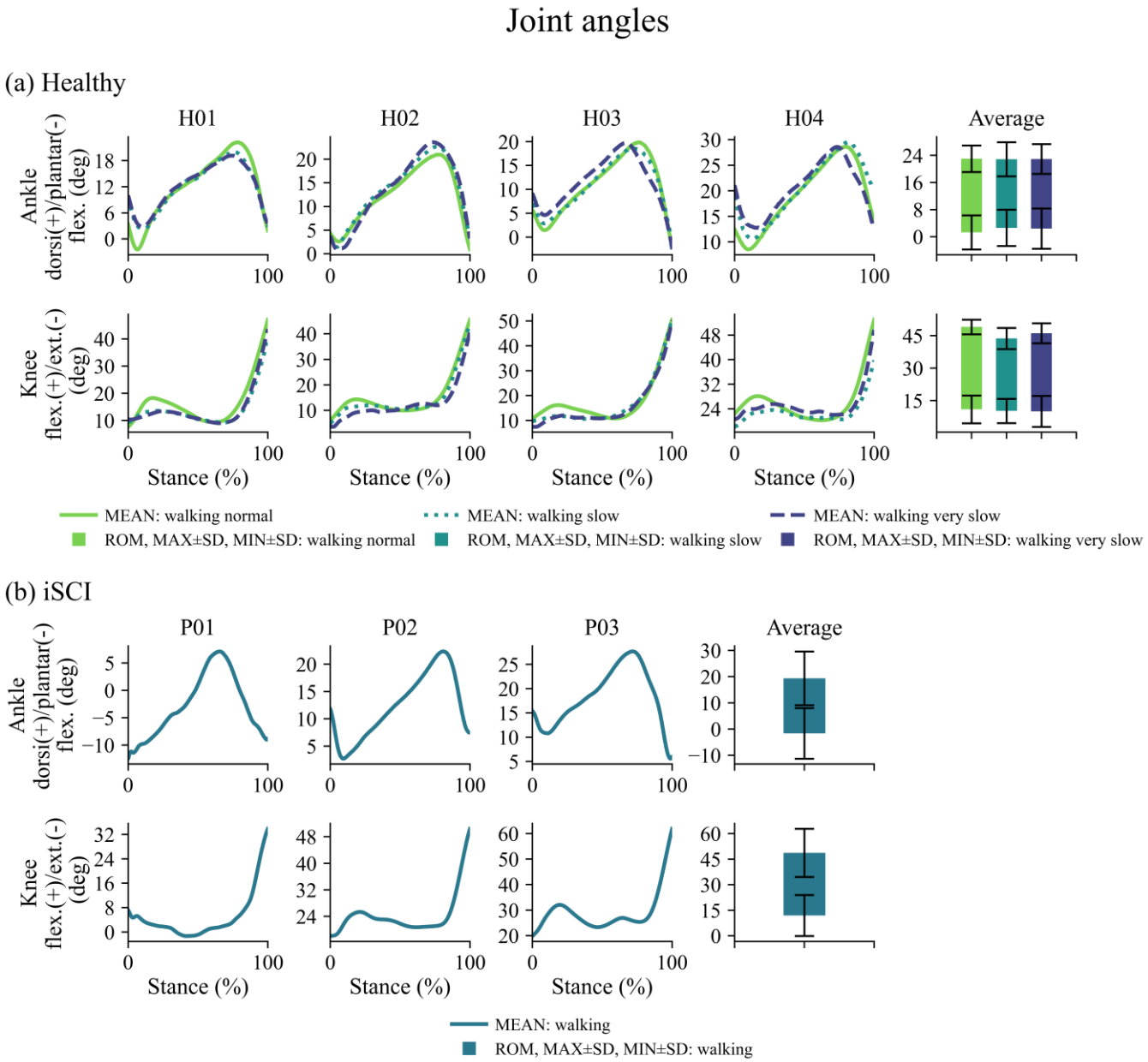

Fig. 4. Results of the joint angle estimation using inverse kinematics analysis. Mean angle trajectories for all walking speeds from individual subjects are displayed for ankle and knee joints. Averaged range of motion (ROM), averaged maximum and minimum of joint angles are represented with their standard deviation. Results are presented for (a) healthy subjects and (b) iSCI subjects.

OpenSim's inverse dynamics analysis. The target joint moments that were included in the calibration process were ankle plantar/dorsi flexion and knee flexion/extension.

Since the number of acquired EMG channels was smaller than that of the available muscle branches in the NMS model, there was a need to define the excitation generator mapping between the EMG input signals and the muscle branches in the NMS model. Table III shows the excitation generator mapping between the EMG input and the NMS model muscle branches. Some modeled muscle branches were assigned to the EMG activation recorded from their closest muscles. For instance, the peroneus tertius in the NMS model used the measured EMG of the tibialis anterior, and the vastus intermedius in the NMS model used the average of the vastus lateralis and vastus medialis EMG measurements. The biceps femoris EMG was used for both its long and short head in the NMS model, and the gastrocnemius medialis EMG was used for both gastrocnemius medialis and gastrocnemius lateralis. All the other muscle branches were removed from the NMS model, except for the 11 muscle branches described in Table III. The fundamental assumption of this approach is that only the muscles for which an excitation is assigned (in Table III) are responsible for the generation of the required joint torques [9]. Since it was not possible to use more than 7 iEMG electrodes in order to avoid potential discomfort of the subjects, it was decided not to use iEMG electrodes around the hip joint muscles, because some of those are located deeply so that the measurement of corresponding sEMG was not possible. Thus, the hip joint torque prediction in the model was eliminated.

For the healthy subjects, 3 trials (walking normal, walking

This article has been accepted for publication in a future issue of this journal, but has not been fully edited. Content may change prior to final publication. Citation information: DOI 10.1109/TBME.2021.3087137, IEEE Transactions on Biomedical Engineering

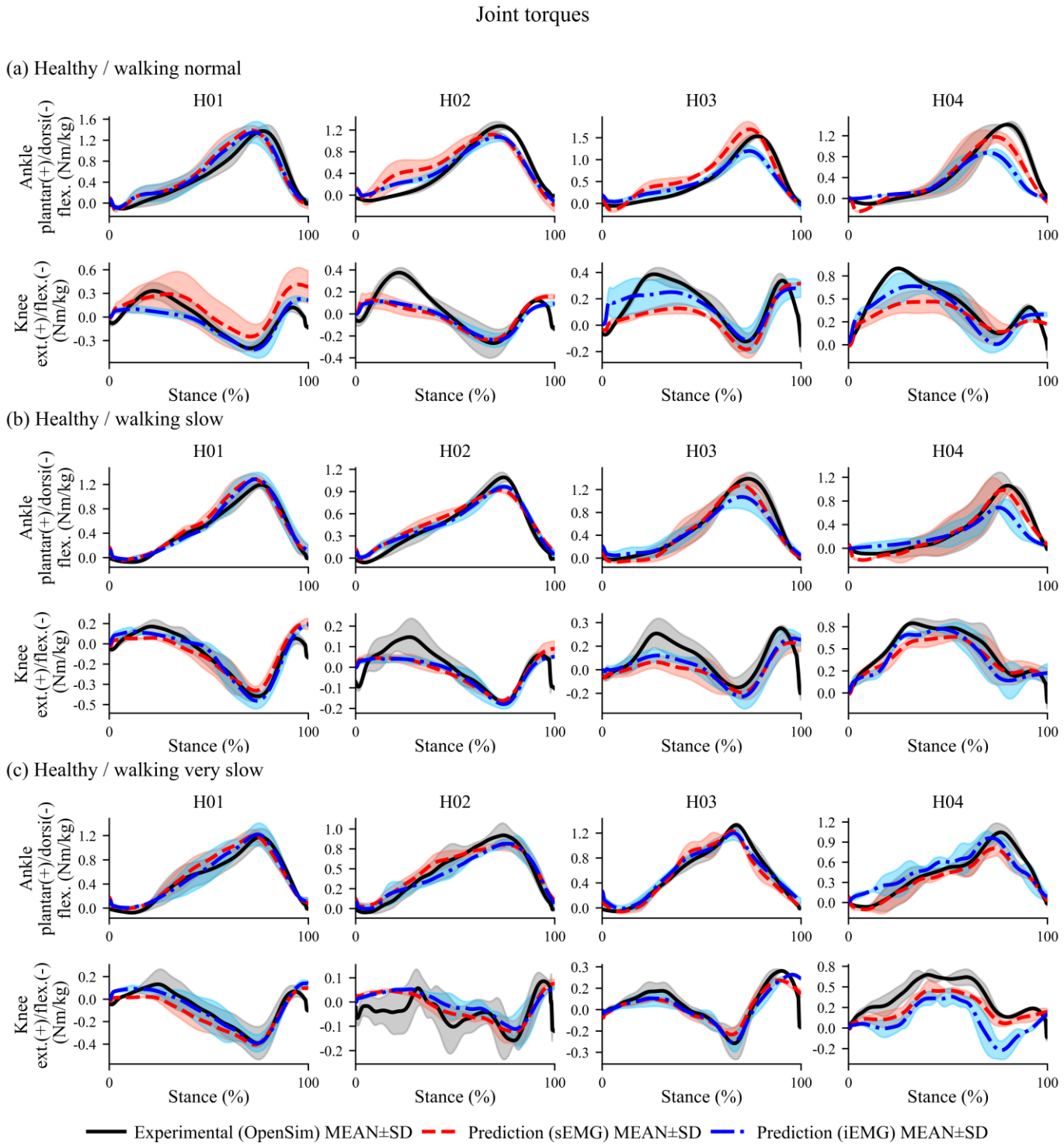

Fig. 5. Joint torque estimation results using the EMG-driven modeling framework for all healthy subjects. Black lines show the mean of the experimental (reference) joint torques evaluated by inverse dynamics analysis in OpenSim. Red lines show the mean of the predicted joint torques using sEMG whereas blue lines show the mean of the predicted joint torques using iEMG. The shaded area shows 1 standard deviation (SD) for each time step during the entire stance phase of walking trials. For each walking speed of a subject, 3 trials were used for the execution of the NMS model (9 trials in total for each subject).

slow, walking very slow) were used for the calibration of each subject. For the iSCI subjects, 3 walking trials were used for each subject.

Two separated NMS models were calibrated for each subject, one for the surface EMG inputs and the other for the intramuscular EMG inputs. After this calibration process, muscle forces and joint moments were estimated from the remaining trials (obtained excluding the calibration trials), 3 trials of each walking speed (9 trials in total for each subject) for healthy subjects, and 7 trials of walking for iSCI subjects.

This article has been accepted for publication in a future issue of this journal, but has not been fully edited. Content may change prior to final publication. Citation information: DOI 10.1109/TBME.2021.3087137, IEEE Transactions on Biomedical Engineering

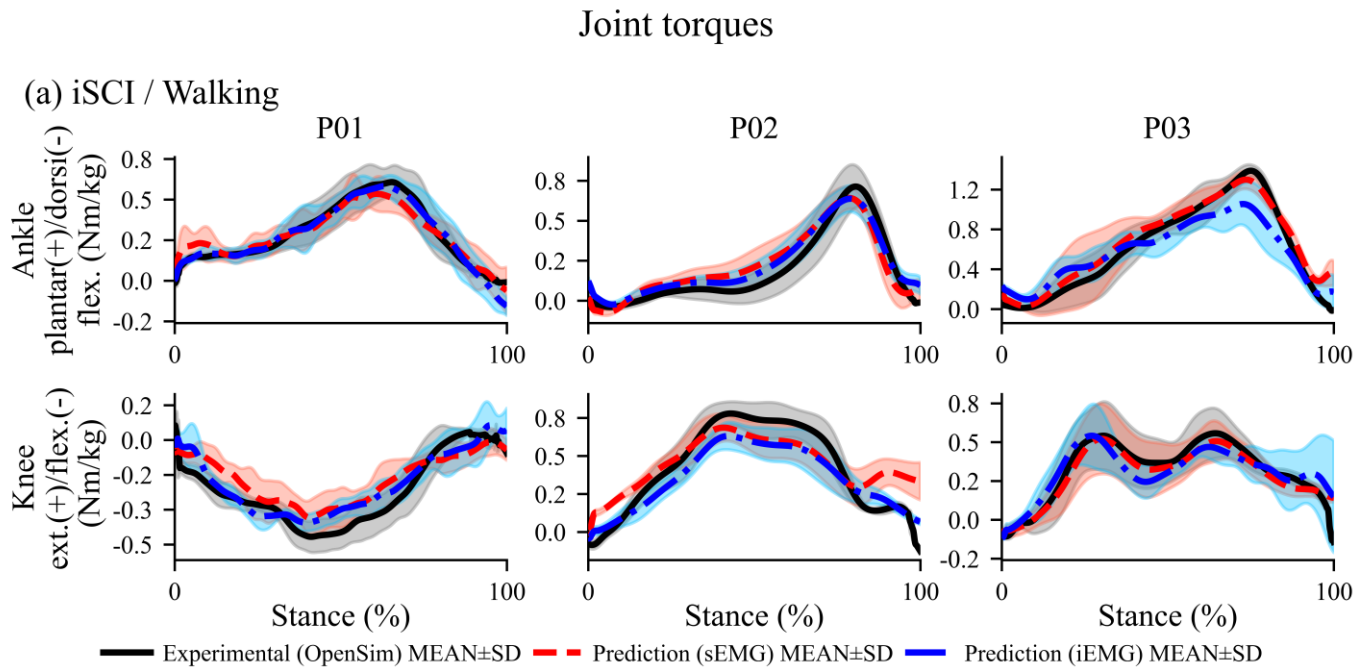

Fig. 6. Joint torque estimation results using the EMG-driven modeling framework for all iSCI subjects. Black lines show the mean of the experimental (reference) joint torques evaluated by inverse dynamics analysis in OpenSim. Red lines show the mean of the predicted joint torques using sEMG whereas blue lines show the mean of the predicted joint torques using iEMG. The shaded area shows 1 standard deviation (SD) for each time step during the entire stance phase of walking trials. For each subject, 7 trials were used for the execution of the NMS model.

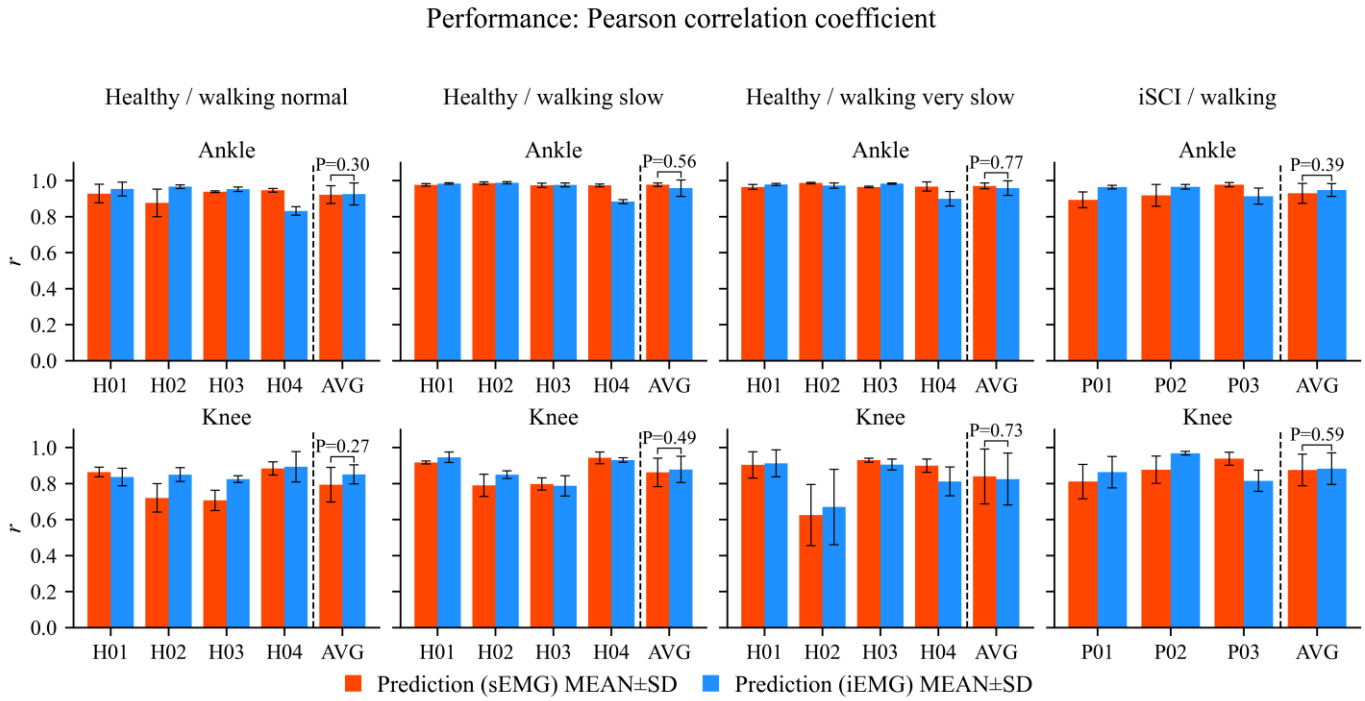

Fig. 7. Performance metrics of joint torque prediction using the EMG-driven modelling framework. Pearson correlation coefficient (r) values were estimated between the experimental (reference) and the predicted joint torques for all the trials from every subject. The heights of colored bars represent the average r values and the error bars the standard deviations.

C. Data analysis

The Pearson correlation coefficient (r) and root-mean-square-error (RMSE) were estimated for the experimental (OpenSim's inverse dynamics) and the predicted (EMG-driven open-loop mode) joint moments. As the performance parameters did not satisfy the normality assumption according to the Shapiro-Wilk test, a nonparametric Kruskal-Wallis test was used to compare the performance of joint moment prediction between sEMG and iEMG. $P < 0.05$ was the threshold for significance. All the data analyses were performed using Python, NumPy and SciPy libraries [29], [30], [31].

This article has been accepted for publication in a future issue of this journal, but has not been fully edited. Content may change prior to final publication. Citation information: DOI 10.1109/TBME.2021.3087137, IEEE Transactions on Biomedical Engineering

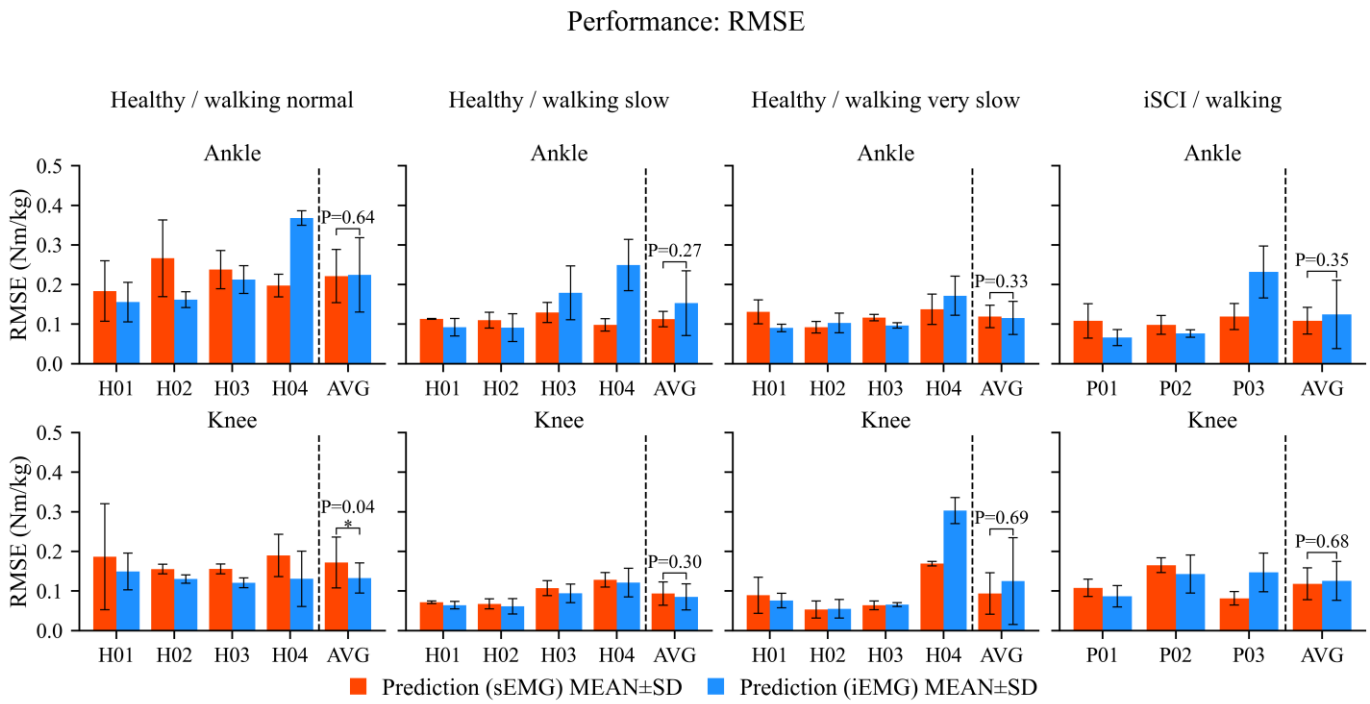

Fig. 8. Performance metrics of joint torque prediction using the EMG-driven modelling framework. Root mean square error (RMSE) values were estimated between the experimental (reference) and the predicted joint torques for all the trials from every subject. The heights of colored bars represent the RMSE values in Nm/kg and their standard deviations are displayed with error bars.

IV. Results

Fig. 3 shows the walking speeds for healthy subjects (walking normal: $0.88 \pm 0.09\, m/s$, walking slow: $0.53 \pm 0.08\, m/s$, walking very slow: $0.36 \pm 0.05\, m/s$) and iSCI patients (average walking speed: $0.41 \pm 0.13\, m/s$). For all trials of both healthy and iSCI subjects, the speed of individual trials was self-paced. Healthy subjects were asked to walk at additional walking speeds (walking slow and walking very slow), in order to mimic the walking speeds of iSCI subjects. The average speed of iSCI subjects' walking trials was in between the average speed of the walking slow and very slow trials of healthy subjects.

The results of the joint angle calculation using the inverse kinematics analysis of OpenSim are summarized in Fig. 4. For healthy subjects, the average range of motion (ROM) values of ankle joint were $21.72 \pm 2.24\,°$, $20.23 \pm 1.13\,°$, $20.50 \pm 2.71\,°$ and the average ROM values of knee joint were $38.14 \pm 3.56\,°$, $33.53 \pm 8.73\,°$, $36.15 \pm 5.59\,°$ for the three walking speeds. For iSCI subjects, the average ROM value of ankle joint was $21.01 \pm 1.42\,°$ and the average ROM value of knee joint was $36.76 \pm 4.85\,°$ for their single walking speed configuration. Fig. 4 shows that the patterns of both knee and ankle joint angles were similar between healthy subjects and iSCI patients. However, there were differences in the minimum and maximum values of those joint angles among the subjects in each group.

Fig. 5 and Fig. 6 show the results of the joint torque estimation using the calibrated EMG-driven NMS models for the healthy and iSCI subjects, respectively. Fig. 7 shows the Pearson correlation coefficient (r) between the experimental (reference) and the predicted joint torques, and Fig. 8 reports the root-mean-square-error (RSME) between the experimental and the predicted joint torques. Table IV shows the summary of the performance metrics comparison between sEMG and iEMG for all cases.

In Fig. 5 and Fig. 6, the results of the joint torque estimation are reported during the stance phase between 0% (heel-strike) and 100% (toe-off). All joint torques were normalized by the masses of the subjects, for consistency with previous studies [7], [8], [9], [11]. The 'body weight times height' joint torque normalization approach was also tested in order to observe the effect of height and weight on the peak values of the joint torques [33]. None of the results significantly changed when we applied this normalization to our data, therefore the body mass normalization only was used for reporting the final results. To create Fig. 5 and Fig. 6, 3 different B-spline curves were constructed in order to interpolate the experimental, the sEMG-driven and the iEMG-driven joint torques, using the entire dataset from the stance phase of each trial. Then the estimation of these curves was performed using the same number of stance phase percentage points in order to replicate the stance phase in the range 0-100%. Because the calibration processes of EMG-driven NMS models were performed using both ankle and knee DOFs, the joint torques of these 2 DOFs were estimated simultaneously [7]. Results show that the estimated joint torques are comparable with the reference (OpenSim's inverse dynamics) torques for both sEMG and iEMG. For healthy subjects (Fig. 5), the normalized ankle plantar-flexion joint torque curves from all cases showed a similar trend, whereas the patterns of the normalized knee extension joint torque curves varied among subjects. A single peak was usually observed for the ankle plantar-flexion joint torque curves

This article has been accepted for publication in a future issue of this journal, but has not been fully edited. Content may change prior to final publication. Citation information: DOI 10.1109/TBME.2021.3087137, IEEE Transactions on Biomedical Engineering

TABLE IV
SUMMARY OF JOINT TORQUE ESTIMATION PERFORMANCE METRICS

		Healthy									iSCI		
		Walking normal			Walking slow			Walking very slow			Walking		
Joint	Metric	sEMG	iEMG	P	sEMG	iEMG	P	sEMG	iEMG	P	sEMG	iEMG	P
Ankle	r±SD	0.92±0.05	0.93±0.06	0.30	0.98±0.01	0.96±0.05	0.56	0.97±0.02	0.96±0.04	0.77	0.93±0.06	0.95±0.04	0.39
	RMSE±SD (Nm/kg)	0.22±0.07	0.22±0.09	0.64	0.11±0.02	0.15±0.08	0.27	0.12±0.03	0.12±0.04	0.33	0.11±0.03	0.12±0.09	0.35
Knee	r±SD	0.79±0.10	0.85±0.05	0.27	0.86±0.08	0.88±0.07	0.49	0.84±0.15	0.83±0.14	0.73	0.88±0.09	0.88±0.09	0.59
	RMSE±SD (Nm/kg)	0.17±0.06	0.13±0.04	0.04	0.09±0.03	0.09±0.03	0.30	0.09±0.05	0.12±0.11	0.69	0.12±0.04	0.13±0.05	0.68

Performance metrics of joint torque estimation using the EMG-driven NMS-model based framework with both sEMG and iEMG.

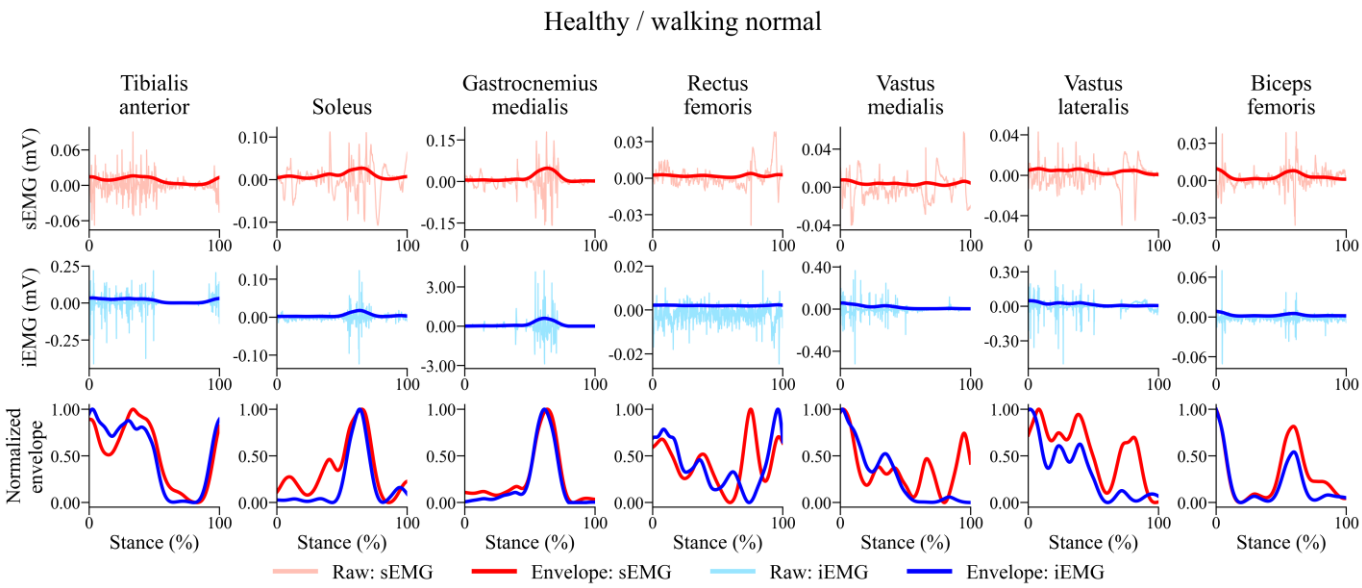

Fig. 9. Representative surface and intramuscular EMG measurements from a healthy subject's walking trial.

whereas two peaks were detected in the knee extension joint torque curves during the stance phase of a gait cycle. For walking at normal speed, the predictions of knee joint torques had greater errors for the first peak than the second. Moreover, for each subject, the peak values of these normalized joint torque curves varied with walking speed.

For iSCI subjects (Fig. 6), the trend of the normalized ankle plantar-flexion joint torque curves was consistent except for the peak magnitudes, whereas the patterns of the normalized knee extension joint torque curves varied substantially among subjects in magnitude and shape. The main reason of different knee extension joint torque patterns may be the different knee joint angle kinematics among these iSCI subjects, as seen in Fig. 4(b). Nevertheless, the predicted ankle and knee joint torques using both sEMG and iEMG driven NMS models showed good agreements with the reference joint torques even though their reference joint torque patterns were not consistent with those of healthy subjects, which indicates the capacity of EMG-driven NMS models to predict the joint torques of patients with pathological gait patterns. In Fig. 6, the results for P01 are more oscillatory than those for P02 and P03. Moreover, in Fig. 3, the walking speed of P01 is much slower than for any other healthy and iSCI subjects. Thus, the trials of P01 have more data points than other trials during the stance phase and for this reason the interpolation results in curves with more oscillations for this patient.

Regarding the joint torque estimation performance, for healthy subjects (Fig. 5, Table IV), the highest r values for sEMG were 0.98 ± 0.01 (ankle) and 0.86 ± 0.08 (knee) when walking at slow speed, whereas the highest r values for iEMG were 0.96 ± 0.05 (ankle) and 0.88 ± 0.07 (knee) when walking at slow speed. The smallest RMSE values for sEMG were 0.11 ± 0.02 Nm/kg (ankle) and 0.09 ± 0.03 Nm/kg (knee) at slow speed, and the smallest RMSE values for iEMG were 0.15 ± 0.08 Nm/kg (ankle) and 0.09 ± 0.03 Nm/kg (knee) at slow speed. For iSCI subjects (Fig. 6, Table IV), the r values for sEMG were 0.93 ± 0.06 (ankle) and 0.88 ± 0.09 (knee), whereas the r values for iEMG were 0.95 ± 0.04 (ankle) and 0.88 ± 0.09 (knee). The RMSE values for sEMG were 0.11 ± 0.03 Nm/kg (ankle) and 0.12 ± 0.04 Nm/kg (knee), whereas the RMSE values for iEMG were 0.12 ± 0.09 Nm/kg (ankle) and 0.13 ± 0.05 Nm/kg (knee). Table IV shows that the r values of ankle joint torque predictions were greater than for knee joint torque prediction. On average, the RMSE values for ankle joint torque prediction were greater than for the knee joint torque prediction for healthy subjects, while the opposite was observed for iSCI patients.

The statistical analysis (Fig. 7 and Fig. 8) of the joint torque estimation performance metrics (r and RMSE) showed that RMSE of the knee extension/flexion torque estimation for iEMG was lower than for sEMG ($P = 0.04 < 0.05$).

Fig. 9 and Fig. 10 show representative cases of data from a healthy subject and an iSCI subject during walking trials. In

This article has been accepted for publication in a future issue of this journal, but has not been fully edited. Content may change prior to final publication. Citation information: DOI 10.1109/TBME.2021.3087137, IEEE Transactions on Biomedical Engineering

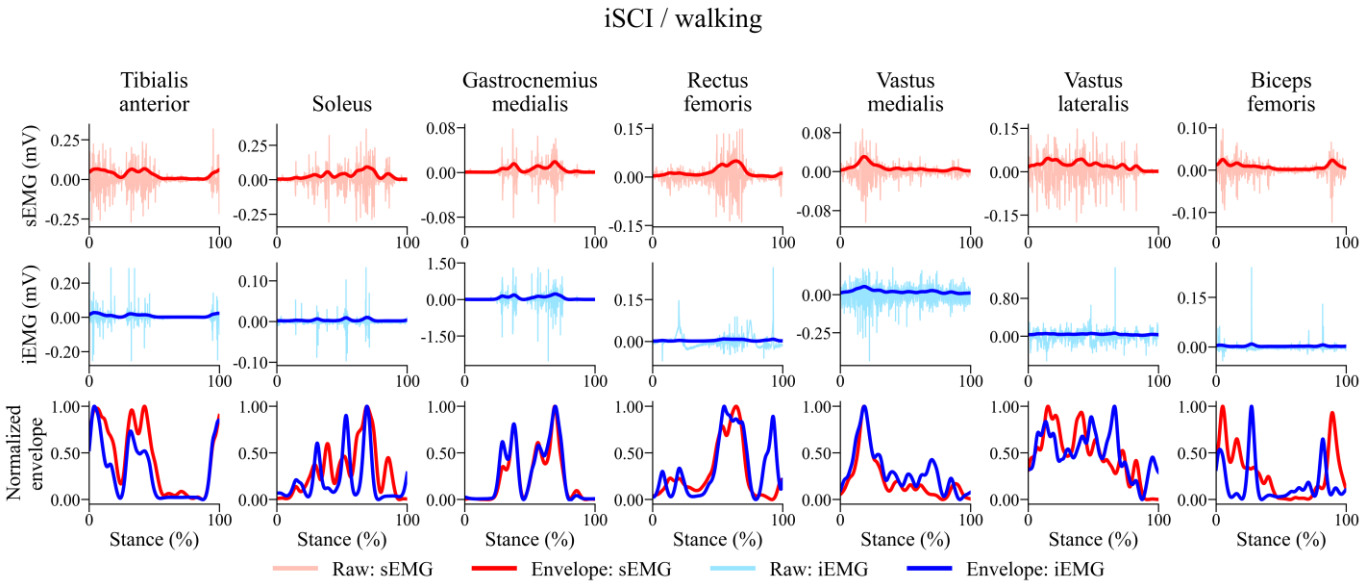

Fig. 10. Representative surface and intramuscular EMG measurements from an iSCI subject's walking trial.

general, EMG linear envelope curves showed good matching between surface and intramuscular EMGs. However, for instance in Fig. 10, rectus femoris, vastus lateralis and biceps femoris had some intermittent spikes in their iEMG measurements. These high spikes in iEMG may result in less accurate normalization of EMG amplitudes and therefore decrease both the accuracy of model calibration and the performance of joint torque prediction.

V. DISCUSSION

We have applied EMG-driven modelling to estimate ankle and knee joint torques from intramuscular or surface EMG signals recorded unilaterally from 7 leg muscles. We have evaluated the approach in healthy individuals and patients with incomplete SCI. The results showed that the correlation between experimental and predicted joint torques was similar when using intramuscular or surface EMG as input to our model. The only difference in performance was for the knee joint torque prediction in healthy subjects walking at normal speed where iEMG resulted in superior performance than sEMG. Because the target population for assistive devices would likely walk slower (see Fig. 3), this difference may have a limited impact in the EMG-driven NMS modeling for the control of exoskeletons. These results show that iEMG can be used as a potential input for NMS model-based joint torque estimation, with performance similar to that of surface EMG.

Previous studies utilized surface EMG-driven joint torque estimates to control either prostheses or wearable assistive devices [12], [13]. Among various control strategies for lower limb exoskeletons [34], it was previously shown that joint torque patterns are similar when walking with robotic assistance with respect to unconstrained walking [35]. For this reason, joint torque estimates obtained from EMG and NMS models can be used for HMI.

Compared to sEMG, iEMG is less affected by crosstalk. However, iEMG signals may contain intermittent spikes and high-frequency components, which may make the estimation of muscle force magnitude and timing less accurate. Moreover, intramuscular EMG electrodes can be highly sensitive to the movement of muscles, and their relative location with respect to muscles may vary according to the duration of the performed task, which may affect normalization. Despite these potential disadvantages, there was no substantial difference in the overall performance of joint torque prediction between sEMG and iEMG.

The advantage of using invasive technology as a source of control of external devices, such as exoskeletons or prostheses, is that it may be applied as a chronic interface, as it has been shown in prosthetic control [16]. In our study we used non-selective fine wires (approximately 1 cm of uninsulated wire) for recording intramuscular EMG. These recordings have similar selectivity to chronically implanted devices (such as the IMES [36]) and can be easily implanted for acute experiments.

Previous studies compared the performance between surface and intramuscular EMGs to predict joint torques/kinematics, but their conclusions were not always consistent. In [20], wrist joint torques were estimated form surface and intramuscular EMGs with artificial neural networks. Surface EMG showed better performance against intramuscular EMG, which may be attributed to the greater selectivity of the iEMG recordings [20]. The main difference of this previous study with respect to ours is that it used untargeted intramuscular EMGs and the approach was based on artificial neural networks (ANN) whereas our study is based on NMS modeling. Another study [21] presented NMS model-based control of a virtual task and reported no differences between surface and intramuscular EMGs. Differently from our study, the works in [20] and [21] focused on the upper limb.

There are potential limitations in this study. First, in many previous studies using offline EMG-driven modeling analysis, the number of EMG channels and NMS model's MTUs were greater than in the current study [7], [8], [9]. In our study, we had to limit the number of channels because of the acute insertion of intramuscular wires. Accordingly, the number of

NMS model's MTU was limited to 11. The main consequence was the absence of hip muscle measurements which hampered the estimation of the joint torques of the hip DOFs. Moreover, it was not possible to include all relevant knee flexor and extensor muscles in the NMS model. Considering that the cross-sectional area of the semitendinosus and semimembranosus is comparable with that of the biceps femoris [37], their omission might have resulted in less accurate tracking of the knee flexion/extension torque in some of the trials in Figs. 5 and 6.

Regarding the muscle excitation mapping described in Table III, several other options of muscle excitation mappings were tested for the calibration of the EMG-driven NMS models but they did not provide significantly different results. Moreover, while we used the same muscle excitation mapping for both healthy and iSCI subjects, a different mapping for the two subject groups may be more appropriate because of the differences in muscle activation patterns in healthy and iSCI subjects [24], [25]. Some recent studies tried to reduce the number of EMG electrodes and NMS model MTUs for applications such as real-time joint torque estimation or control of wearable robotic exoskeletons [12], [13]. Second, this study analyzed walking trials only. This was mainly due to the constraints of measurements in SCI patients.

While the iSCI subjects that participated in this study had the same AIS score, their lesion levels were different, and their compensatory movements might have been different. This may explain the high standard deviation observed in Fig. 8.

Finally, only data from the stance phase was reported in the results. The main reason for this choice is that both ankle and knee joint torques are highest during the stance phase, whereas the swing phase is mainly determined by the hip joint torque. Moreover, the experimental setup included only two force plates for the detection of heel strike and toe off, thus the second heel strike could not be accurately detected. For similar reasons, many previous EMG-driven NMS studies for lower limbs did not report the results during the swing phase [7], [8], [9], [11]. However, having the results of the full gait cycle may be important for the control of exoskeletons, which need to modulate both stand and swing phases. The most effective way to increase the performance of EMG-driven NMS models is to increase the number of EMG recordings. Our EMG-driven NMS model runs in open-loop mode, and its main purpose is to estimate the user-intended joint torque for target joints. Thus, predictions may be in principle improved also by a multi-modal or a hybrid approach, with additional information, for example with the use of additional wearable sensors.

VI. CONCLUSION

We have shown that intramuscular EMG can be used as a proper input for NMS model based joint torque estimation. This study also shows the potential use of both surface and intramuscular EMG measurements for NMS models with a reduced number of EMG acquisition channels in both healthy and iSCI subjects. These results indicate the potential use of intramuscular EMG as a reliable input for HMIs.

ACKNOWLEDGMENT

The authors would like to thank Enrique Pérez Rizo, Natalia Comino Suárez and María Isabel Sinovas Alonso for their assistance on the experimental and data acquisition procedure.

REFERENCES

[1] D. Farina et al. (2017). Man/machine interface based on the discharge timings of spinal motor neurons after targeted muscle reinnervation. Nature biomedical engineering, 1(2), 1-12.

[2] J. R. Koller et al. (2015). Learning to walk with an adaptive gain proportional myoelectric controller for a robotic ankle exoskeleton. Journal of neuroengineering and rehabilitation, 12(1), 1-14.

[3] S. Muceli and D. Farina. (2011). Simultaneous and proportional estimation of hand kinematics from EMG during mirrored movements at multiple degrees-of-freedom. IEEE transactions on neural systems and rehabilitation engineering, 20(3), 371-378.

[4] N. Jiang et al. (2012). EMG-based simultaneous and proportional estimation of wrist/hand kinematics in uni-lateral trans-radial amputees. Journal of neuroengineering and rehabilitation, 9(1), 42.

[5] D. G. Lloyd and T. F. Besier. (2003). An EMG-driven musculoskeletal model to estimate muscle forces and knee joint moments in vivo. Journal of biomechanics, 36(6), 765-776.

[6] T. S. Buchanan et al. (2004). Neuromusculoskeletal modeling: estimation of muscle forces and joint moments and movements from measurements of neural command. Journal of applied biomechanics, 20(4), 367-395.

[7] M. Sartori et al. (2012). EMG-driven forward-dynamic estimation of muscle force and joint moment about multiple degrees of freedom in the human lower extremity. PloS one, 7(12), e52618.

[8] M. Sartori et al. (2014). Hybrid neuromusculoskeletal modeling to best track joint moments using a balance between muscle excitations derived from electromyograms and optimization. Journal of biomechanics, 47(15), 3613-3621.

[9] C. Pizzolato et al. (2015). CEINMS: A toolbox to investigate the influence of different neural control solutions on the prediction of muscle excitation and joint moments during dynamic motor tasks. Journal of biomechanics, 48(14), 3929-3936.

[10] D. L. Crouch and H. H. Huang. (2017). Musculoskeletal model-based control interface mimics physiologic hand dynamics during path tracing task. Journal of neural engineering, 14(3), 036008.

[11] G. Durandau et al. (2018). Robust real-time musculoskeletal modeling driven by electromyograms. IEEE transactions on biomedical engineering, 65(3), 556-564.

[12] M. Sartori et al. (2018). Robust simultaneous myoelectric control of multiple degrees of freedom in wrist-hand prostheses by real-time neuromusculoskeletal modeling. Journal of neural engineering, 15(6), 066026.

[13] G. Durandau et al. (2019). Voluntary control of wearable robotic exoskeletons by patients with paresis via neuromechanical modeling. Journal of neuroengineering and rehabilitation, 16(1), 91.

[14] D. Buongiorno et al. (2018). A linear approach to optimize an EMG-driven neuromusculoskeletal model for movement intention detection in myo-control: A case study on shoulder and elbow joints. Frontiers in neurorobotics, 12, 74.

[15] M. Ortiz-Catalan et al. (2014). An osseointegrated human-machine gateway for long-term sensory feedback and motor control of artificial limbs. Science translational medicine, 6(257), 257re6-257re6.

[16] L. Hargrove et al. (2006, August). The effect of electrode displacements on pattern recognition based myoelectric control. In 2006 International Conference of the IEEE Engineering in Medicine and Biology Society (pp. 2203-2206). IEEE.

[17] A. J. Young et al. (2011). The effects of electrode size and orientation on the sensitivity of myoelectric pattern recognition systems to electrode shift. IEEE Transactions on Biomedical Engineering, 58(9), 2537-2544.

[18] S. Salminger et al. (2019). Long-term implant of intramuscular sensors and nerve transfers for wireless control of robotic arms in above-elbow amputees. Science Robotics, 4(32).

[19] M. M. Lowery et al. (2006). Simulation of intramuscular EMG signals detected using implantable myoelectric sensors (IMES). IEEE transactions on biomedical engineering, 53(10), 1926-1933.

[20] E. N. Kamavuako et al. (2013). Wrist torque estimation during simultaneous and continuously changing movements: surface vs.

untargeted intramuscular EMG. Journal of neurophysiology, 109(11), 2658-2665.

[21] D. L. Crouch et al. (2018). Comparing surface and intramuscular electromyography for simultaneous and proportional control based on a musculoskeletal model: A pilot study. IEEE Transactions on Neural Systems and Rehabilitation Engineering, 26(9), 1735-1744.

[22] A. Péter et al. (2019). Comparing surface and fine-wire electromyography activity of lower leg muscles at different walking speeds. Frontiers in physiology, 10, 1283.

[23] A. Kian et al. (2019). Static optimization underestimates antagonist muscle activity at the glenohumeral joint: A musculoskeletal modeling study. Journal of biomechanics, 97, 109348.

[24] P. Wang et al. (2013). Detection of abnormal muscle activations during walking following spinal cord injury (SCI). Research in developmental disabilities, 34(4), 1226-1235.

[25] S. Pérez-Nombela et al. (2017). Modular control of gait after incomplete spinal cord injury: differences between sides. Spinal Cord, 55(1), 79-86.

[26] S. L. Delp et al. (2007). OpenSim: open-source software to create and analyze dynamic simulations of movement. IEEE transactions on biomedical engineering, 54(11), 1940-1950.

[27] K. Monaghan et al. (2007). Increasing the number of gait trial recordings maximises intra-rater reliability of the CODA motion analysis system. Gait & posture, 25(2), 303-315.

[28] J. Stebbins et al. (2006). Repeatability of a model for measuring multi-segment foot kinematics in children. Gait & posture, 23(4), 401-410.

[29] T. E. Oliphant. (2007). Python for scientific computing. Computing in Science & Engineering, 9(3), 10-20.

[30] C. R. Harris et al. (2020). Array programming with NumPy. Nature, 585(7825), 357-362.

[31] P. Virtanen et al. (2020). SciPy 1.0: fundamental algorithms for scientific computing in Python. Nature methods, 17(3), 261-272.

[32] W. L. Goffe et al. (1994). Global optimization of statistical functions with simulated annealing. Journal of econometrics, 60(1-2), 65-99.

[33] K. C. Moisio et al. (2003). Normalization of joint moments during gait: a comparison of two techniques. Journal of biomechanics, 36(4), 599-603.

[34] T. Yan et al. (2015). Review of assistive strategies in powered lower-limb orthoses and exoskeletons. Robotics and Autonomous Systems, 64, 120-136.

[35] P. C. Kao et al. (2010). Invariant ankle moment patterns when walking with and without a robotic ankle exoskeleton. Journal of biomechanics, 43(2), 203-209.

[36] R. F. Weir et al. (2003, September). Implantable myoelectric sensors (IMES) for upper-extremity prosthesis control-preliminary work. In Proceedings of the 25th Annual International Conference of the IEEE Engineering in Medicine and Biology Society (IEEE Cat. No. 03CH37439) (Vol. 2, pp. 1562-1565). IEEE.

[37] A. Kositsky et al. (2020). Reliability and validity of ultrasonography for measurement of hamstring muscle and tendon cross-sectional area. Ultrasound in medicine & biology, 46(1), 55-63.